

Autofocusing and Self-Healing Properties of Aberration Laser Beams in a Turbulent Media

Vasu Dev¹, Andra Naresh K. Reddy^{2,3}, Andrey V. Ustinov⁴, Svetlana N. Khonina^{4,5} and Vishwa Pal^{1,*}


¹*Department of Physics, Indian Institute of Technology Ropar, Rupnagar, Punjab 140001, India*

²*Department of Physics of Complex Systems, Weizmann Institute of Science, Rehovot 7610001, Israel*

³*Anurag University, Venkatapur, Hyderabad, Telangana 500 088, India*

⁴*Image Processing Systems Institute of RAS—Branch of the FSRC “Crystallography and Photonics” RAS, 151 Molodogvardeyskaya Str., Samara 443001, Russia*

⁵*Samara National Research University, Samara 443086, Russia*

 (Received 26 March 2021; revised 28 May 2021; accepted 29 June 2021; published 27 July 2021)

We present the autofocusing and self-healing properties of aberration laser beams (ALBs) in a turbulent media. The ALB is generated by a diffractive optical element (DOE) whose phase profile consists of radial and periodic angular dependence, and then propagated through a turbulent media under weak, moderate, and strong turbulence conditions. The theoretical calculations, numerical simulations, and experimental results are presented. The results show that the presence of turbulence leads to distortion in the spatial structure of ALBs, as well as causes beam wandering. However, the autofocusing properties of ALBs remain invariant. Further, ALBs also possess self-healing abilities in free space as well as in a turbulent media. The self-healing sustains reasonably well even when a large portion of ALB (approximately 60%) is truncated. The distance requires for the self-healing of truncated ALBs remains the same for various percentage of truncation. Particularly, for any amount of truncation up to approximately 60%, ALB self-heals by propagating up to autofocusing distance corresponding to a nontruncated beam.

DOI: [10.1103/PhysRevApplied.16.014061](https://doi.org/10.1103/PhysRevApplied.16.014061)

I. INTRODUCTION

The aberration laser beams (ALBs), possessing autofocusing and self-healing properties with turbulence resilience have attracted considerable interests due to their applications in various fields, such as in optical communications, imaging, and investigation of the biomedical materials and examination of small complex biological samples or tissues, ablation, trapping, and guiding the microparticles, and material processing [1–5]. Generally, the term aberration refers to an error (distortions) in the phase front of an optical field. It is well known that the presence of aberration in an optical system affects the quality of imaging and focusing properties of the system [6]. Aberration can cause various symmetric and asymmetric adverse effects like blurring, widening, and distortion in an optical field, and for the minimization of these effects various methods have been proposed [7–9]. However, aberration has also been deliberately exploited for various purposes. For example, the presence of a certain type of aberration in an optical system has been shown to increase the sharp focusing features of an imaging system [10,11]. Several

other studies have also demonstrated the use of aberrations for the generation of diffraction-free laser beams [12], identification of the order of singularity in vortex fields [13–15], and formation of a dark spot on the focal plane [16].

Recently, ALBs have been shown to exhibit autofocusing properties in a free space [17], and their spectral dependence was also investigated [18]. The autofocusing properties of accelerating fields like hypergeometric beams and circular Airy beams have also been investigated [19,20]. In addition to these, several other works have also studied these aspects in different kinds of optical fields [1,21–23].

In various applications, laser beams are required to propagate through a random or disordered media. The propagation of laser beam through a random media encounters various effects like scattering, intensity fluctuations, attenuation of beam, loss of coherence, and localization [24–26]. Although, scattering is a primary phenomenon in random media, these scattering and intensity fluctuations can be controlled by introducing disorder-specific active components to the medium [27]. Atmospheric turbulence can be considered as a disordered media having random fluctuations in the refractive index and wind velocity due

*vishwa.pal@iitpr.ac.in

to uncertain variations in the temperature gradient of the medium [28]. Although, several works have been carried out to study the propagation of light through random media. However, the field is still growing to better understand the propagation of structured light in random media of different strengths [29,30]. The turbulent propagation of vortex beams (Laguerre-Gaussian and Bessel) reveals that the region of zero intensity is maintained during the propagation with less spreading and shape stability is more for higher topological charges [31–33]. For the Airy beams, it is shown that the position of the centroid and skewness does not depend on turbulence [34].

Recently nondiffracting optical beams, called pinlike optical beams, have been investigated, and it has been shown that these beams show autofocusing after a certain distance and convert to Bessel beam that remains invariant upon further propagation [2,3]. The invariant propagation characteristic was also shown in turbulent media for longer distances. Further, these invariant characteristics were also compared with abruptly autofocused beams [3]. The width of the main lobe of these beams was shown to be inversely proportional to propagation distance, so a tight focusing of energy can be obtained over a long distance. Further, the linearly and circularly polarized circular Airy beams are shown to possess the robust autofocusing properties against strong disturbance by large sized particles, and found to be a decent candidate for trapping and guiding the microparticles [5,35]. In topological beams (Laguerre-Gaussian and Bessel) atmospheric turbulence induces a cross talk between the modes, making them inadequate for free space optical communication. However, it has been shown that the autofocused beams can overcome such effects for free-space optical communications [4]. Although, several works have reported various kinds of autofocused and nondiffracting beams, such as pinlike optical beams and abruptly focused beams [1–3,5,35]. However, with these autofocused beams, several aspects such as easily controlled tuning of autofocusing position from small to large values, self-healing abilities in free space as well as in turbulent media, and spectral dependence of autofocusing have not been explored in great detail.

In this paper, we present the investigations on the propagation (autofocusing) and self-healing properties of ALBs in turbulent media. In Sec. II, we present a detailed analytical modeling of propagation of ALBs through turbulent media. In Sec. III, the numerical and experimental results are presented for the propagation of ALBs in turbulent media under weak, moderate, and strong turbulence conditions. The quantification of autofocusing distance for various turbulent strength is performed by analyzing the overlap integral. In Sec. IV, we present the spectral dependence of autofocusing properties of ALB in a turbulent medium. In Secs. V and VI, we present the self-healing properties of ALBs in free space as well as in turbulent

media, respectively. Finally, in Sec. VII, we present the concluding remarks.

II. THEORETICAL DESCRIPTION

The optical field of an ALB can be given as [17,18]

$$E(r, \theta) = A(r) \exp[-i\alpha r^q + i \sin(m\theta)], \quad r \leq R. \quad (1)$$

Here $A(r) = \exp(-r^2/2\sigma^2)$ denotes a Gaussian with beam waist σ , m is an integer, which controls the lobe structure in the ALB, R is the radius of a circular aperture, q is radial power, α is a scale parameter having unit mm^{-q} . In free space, for such ALB the autofocusing distance can be given as [18]

$$z_{\max} \approx \frac{2\pi}{q\alpha\lambda(2\sigma/3)^{q-2}}, \quad (2)$$

where λ is the wavelength. As seen from Eq. (2), the autofocusing distance can be varied by different parameters, however dependence on α is the simplest and most convenient to manage. α is a scale parameter that controls the steepness of the aberrated wave front [Eq. (1)]. The high value of α results in greater steepness in the wave front, and autofocusses the beam at shorter propagation distances. Note, the value of m [as given in Eq. (1)] controls the number of lobes in the ALB, and does not affect the autofocusing distance. For various applications, optical field requires propagation through a disordered media. For example, when an optical field propagates through a typical atmosphere, it encounters various random temperature fluctuations in its optical path. These random temperature fluctuations result in random variation in the refractive index of the medium, which leads to the distortion in wave front of the propagated optical field. The Kolmogorov model for atmospheric turbulence gives an appropriate description for such random variation in the refractive index of the medium [28,30,36]. So, we propagate ALB through such a turbulent medium using an extended Huygens-Fresnel principle [28,37].

$$\begin{aligned} E(\rho, \phi, z) = & -\frac{ik_0}{2\pi z} \exp(ik_0 z) \exp\left(\frac{ik_0}{2z}\rho^2\right) \\ & \times \iint E(r, \theta) \exp\left(\frac{ik_0}{2z}r^2\right) \\ & \times \exp\left(-\frac{ik_0}{z}\rho r \cos(\theta - \phi)\right) \\ & \times \exp[\psi(\rho, r, z)] r dr d\theta, \end{aligned} \quad (3)$$

where (r, θ) and (ρ, ϕ) represent coordinates of source and observation (output) planes, respectively, separated by a distance z . $k_0 = 2\pi/\lambda$ represents the wave number of an optical field in free space. $\psi(\rho, r, z)$ represents a random

complex phase function describing the irregularities of turbulent medium. The average intensity at the output plane is given by

$$\langle I(\rho, \phi, z) \rangle = \langle E(\rho, \phi, z) E^*(\rho, \phi, z) \rangle, \quad (4)$$

where $\langle \cdot \rangle$ represents an ensemble averaging over different realizations of random phase screens corresponding to turbulent medium. Using Eqs. (3) and (4), the expression for the averaged intensity at the output plane can be given as:

$$\begin{aligned} \langle I(\rho, \phi, z) \rangle &= \left(\frac{k_0}{2\pi z} \right)^2 \iiint \iiint E(r, \theta) E^*(r', \theta') \\ &\times \exp\left(\frac{ik_0}{2z}(r^2 - r'^2)\right) \exp\left(-\frac{ik_0}{z}r\rho \cos(\phi - \theta)\right) \\ &\times \exp\left(\frac{ik_0}{z}r'\rho \cos(\phi - \theta')\right) \\ &\times \langle \exp[\psi(\rho, r, z) + \psi^*(\rho, r', z)] \rangle rr' dr dr' d\theta d\theta'. \end{aligned} \quad (5)$$

The last term in Eq. (5) describes the correlation of random fluctuations, and can be expressed as [29,37]

$$\begin{aligned} \langle \exp[\psi(\rho, r, z) + \psi^*(\rho, r', z)] \rangle &= \exp(-0.5D_\psi) \\ &= \exp\left(-\frac{(r - r')^2}{l(z)^2}\right). \end{aligned} \quad (6)$$

D_ψ represents the phase structure function in Rytov's representation, and $l(z)$ is the coherence length of the spherical wave propagating in a turbulent medium [29,37]. In a turbulent medium $l(z) = (0.545C_n^2 k_0^2 z)^{-3/5}$, where C_n^2 denotes the structure constant of medium. Generally, the analytical calculation of the intensity from Eq. (5) is very difficult. However, the calculation of intensity on the optical axis becomes relatively simple. Thus, substituting $\rho = 0$ (for optical axis intensity) as well as optical field from Eq. (1), Eq. (5) can be written as

$$\begin{aligned} \langle I(\rho = 0, z) \rangle &= \left(\frac{k_0}{2\pi z} \right)^2 \iiint \iiint \exp\left(-\frac{r^2 + r'^2}{2\sigma^2}\right) \\ &\times \exp\left(-\frac{(r - r')^2}{l(z)^2}\right) \exp[-i\alpha r^q + i \sin(m\theta)] \\ &\times \exp[+i\alpha r'^q - i \sin(m\theta')] \\ &\times \exp\left(\frac{ik_0}{2z}(r^2 - r'^2)\right) rr' dr dr' d\theta d\theta'. \end{aligned} \quad (7)$$

The expression in Eq. (7) is now factorized into angular and radial parts as

$$\begin{aligned} \langle I(\rho = 0, z) \rangle &= \left(\frac{k_0}{2\pi z} \right)^2 \int_0^{2\pi} \exp[i \sin(m\theta)] d\theta \int_0^{2\pi} \\ &\times \exp[-i \sin(m\theta')] d\theta' \int_0^R \int_0^R \exp\left(-\frac{r^2 + r'^2}{2\sigma^2}\right) \\ &\times \exp\left(-\frac{(r - r')^2}{l(z)^2}\right) \exp\left(\frac{ik_0}{2z}(r^2 - r'^2)\right) \\ &\times \exp[-i\alpha(r^q - r'^q)] rr' dr dr'. \end{aligned} \quad (8)$$

Note that only the factor $\exp\{-[(r - r')^2/l(z)^2]\}$ prevents the separability of the radial part in Eq. (8). Moreover, for $l(z) \rightarrow \infty$ (completely coherent case) this factor is equal to unity, and factorization occurs, as it should be in the coherent case. The integrals over the angles θ and θ' are the same and equal to $2\pi J_0(1)$ regardless of m . If the radius of the aperture R satisfies the inequality $R > 2\sigma$ then without the loss of accuracy, an upper limit can be replaced by $+\infty$. Nevertheless, the exact solution of the above expression [Eq. (8)] is not easy to get. Therefore, we apply a stationary-phase method for the analysis of the expression in Eq. (8).

A. Simple application of the stationary-phase method

In this case, we assume that all real factors are slowly varying. Thus, the radial part in Eq. (8) can be represented as follows:

$$\begin{aligned} T(z) &= \int_0^R \int_0^R \exp\left(-\frac{r^2 + r'^2}{2\sigma^2}\right) \exp\left(-\frac{(r - r')^2}{l(z)^2}\right) \\ &\times \exp\left(\frac{ik_0}{2z}(r^2 - r'^2)\right) \exp[-i\alpha(r^q - r'^q)] rr' dr dr' \\ &\approx \int_0^\infty \int_0^\infty A(r, r'; \sigma, l) \exp[i\psi(r, r'; z)] dr dr', \end{aligned} \quad (9)$$

where

$$A(r, r'; \sigma, l) = \exp\left(-\frac{r^2 + r'^2}{2\sigma^2}\right) \exp\left(-\frac{(r - r')^2}{l(z)^2}\right) rr'. \quad (10)$$

$$\psi(r, r'; z) = -\alpha r^q + \frac{k_0}{2z} r^2 + \alpha r'^q - \frac{k_0}{2z} r'^2. \quad (11)$$

The inseparable factor is in the amplitude [Eq. (10)], and the phase is factorized [Eq. (11)], therefore the mixed derivative of the phase is zero. Therefore, the integral in

Eq. (9) can be approximated in a simple form:

$$T(z) \approx \pi A(r_0, r'_0; \sigma, l) \left[\left| \frac{\partial^2 \psi(r_0; z)}{\partial r^2} \frac{\partial^2 \psi(r'_0; z)}{\partial r'^2} \right| \right]^{-1/2}, \quad (12)$$

where r_0 and r'_0 are stationary points. To solve it, we need to find the stationary points as well as the second derivatives.

$$\begin{aligned} \frac{\partial \psi(r, r'; z)}{\partial r} &= -\alpha q r^{q-1} + \frac{k_0}{z} r = 0 \\ \Rightarrow r_0 &= \left(\frac{k_0}{\alpha q z} \right)^{1/(q-2)}, \end{aligned} \quad (13a)$$

$$\begin{aligned} \frac{\partial \psi(r, r'; z)}{\partial r'} &= \alpha q r'^{q-1} - \frac{k_0}{z} r' = 0 \\ \Rightarrow r'_0 &= \left(\frac{k_0}{\alpha q z} \right)^{1/(q-2)}. \end{aligned} \quad (13b)$$

$$\frac{\partial^2 \psi(r_0; z)}{\partial r^2} = -\frac{k_0}{z} (q-2), \quad (14a)$$

$$\frac{\partial^2 \psi(r'_0; z)}{\partial r'^2} = \frac{k_0}{z} (q-2). \quad (14b)$$

Thus, the expression in Eq. (12) has the following explicit form:

$$T(z) \approx \frac{\pi z}{k_0 |q-2|} \exp\left(-\frac{r_0^2}{\sigma^2}\right) r_0^2. \quad (15)$$

The main disadvantage of the obtained expression [Eq. (15)] is that there is no dependence on the coherence length $l(z)$ (turbulent media). The resulting expression for the intensity as a zero approximation can now be given as

$$\begin{aligned} \langle I(0, z) \rangle &= \frac{\pi}{|q-2|} J_0^2(1) \frac{k_0}{z} \left(\frac{k_0}{\alpha q z} \right)^{2/(q-2)} \\ &\times \exp\left[-\left(\frac{k_0}{\alpha q z} \right)^{2/(q-2)} \times \frac{1}{\sigma^2} \right]. \end{aligned} \quad (16)$$

As can be seen, Eq. (16) has a singularity at $q = 2$, which is explained from the physical point of view as follows: the used propagation operator corresponds to the expansion in parabolic waves, therefore the operator's kernel has a quadratic dependence on the radius. In this regard, a converging parabolic wave front ($q = 2$ corresponds to a parabolic lens) is special in this situation and is discussed in more detail below.

Above, we do not take into account the presence of an entrance pupil of radius R . If we take it into account, then in

certain areas there will be shadows, so the obtained expressions will work correctly in the following areas [17,18]:

$$z < \frac{k_0}{\alpha q R^{(q-2)}}, \quad (q < 2), \quad (17a)$$

$$z > \frac{k_0}{\alpha q R^{(q-2)}}, \quad (q > 2). \quad (17b)$$

It can be seen that the boundary of the shadow is determined by one formula, but the location of the shadow area depends on the degree of q . Note, even a rough approximation [Eq. (16)] allows finding the position of intensity maximum, and thereby the autofocusing distance. Discarding the factors, that are independent of z , Eq. (16) can be written as

$$\langle I(0, z) \rangle \approx z^{q/(2-q)} \exp\left(-\mu z^{2/(2-q)}\right), \quad (18)$$

where $\mu = \left(k_0 \sigma^{2-q} / \alpha q\right)^{2/q-2}$. It can be shown that for any q , the on-axis intensity [Eq. (18)] tends to zero at $z \rightarrow 0$ and at $z \rightarrow \infty$. The intensity maximum is reached at $z_{\max} = (q/2\mu)^{(2-q)/2}$ or, explicitly at

$$z_{\max} = \left(\frac{q}{2}\right)^{(2-q)/2} \times \frac{k_0}{\alpha q \sigma^{q-2}}. \quad (19)$$

To prevent the intensity maximum falling into the shadow region, in addition to $R > 2\sigma$, it is necessary to satisfy the inequality

$$R > \sigma \sqrt{\frac{q}{2}}. \quad (20)$$

B. Complicated application of the stationary-phase method

As we see above, the final expression of on-axis intensity [Eq. (16)] does not contain the dependence on $l(z)$ (turbulent medium), so we apply the stationary-phase method more flexibly. Namely, we replace the phases with quadratic expansions, replace the first powers of r and r' with stationary values r_0 , and r'_0 , respectively, but leave the real exponents in their original form. Then we get an expression for integral in Eq. (8) in the form:

$$\begin{aligned} T(z) &\approx \int_0^R \int_0^R \exp\left(-\frac{r^2 + r'^2}{2\sigma^2}\right) \exp\left(-\frac{(r-r')^2}{l(z)^2}\right) \\ &\times \exp\left[i\left(\psi(r_0; z) + \frac{\partial^2 \psi(r_0; z)}{\partial r^2} \frac{(r-r_0)^2}{2}\right)\right] \\ &\times \exp\left[i\left(\psi(r'_0; z) + \frac{\partial^2 \psi(r'_0; z)}{\partial r'^2} \frac{(r'-r'_0)^2}{2}\right)\right] \\ &\times r_0 r'_0 dr dr', \end{aligned} \quad (21)$$

where

$$\psi(r_0; z) = \frac{k_0 r_0^2 (q-2)}{2qz} \quad \text{and} \quad \psi(r'_0; z) = -\frac{k_0 r_0'^2 (q-2)}{2qz}. \quad (22)$$

Let us take into account that $r_0 = r'_0$ [see Eq. (13)], then $\psi(r_0; z) = -\psi(r'_0; z)$. In addition, from Eq. (14) we get $\partial^2 \psi(r_0; z) / \partial r^2 = -[\partial^2 \psi(r'_0; z) / \partial r'^2]$. Then the integral in Eq. (21) takes the following form:

$$T(z) \approx r_0^2 \int_0^R \int_0^R \exp\left(-\frac{r^2 + r'^2}{2\sigma^2} - \frac{(r-r')^2}{l(z)^2}\right) \times \exp\left\{\frac{i}{2} \frac{\partial^2 \psi(r_0; z)}{\partial r^2} [(r-r_0)^2 - (r'-r_0)^2]\right\} dr dr'. \quad (23)$$

After simplification, the integral [Eq. (23)] is solved and substituted to Eq. (8) to obtain a simplified form that is convenient for the analysis.

$$\langle I(0, z) \rangle = \left(\frac{k_0}{\alpha q z}\right)^{2/(q-2)} \frac{2\pi J_0^2(1) k_0^2 \sigma^2}{z \times \sqrt{z^2 \left(1 + \frac{4\sigma^2}{l(z)^2}\right) + k_0^2 \sigma^4 (q-2)^2}} \exp\left[-\left(\frac{k_0}{\alpha q z}\right)^{2/(q-2)} \frac{1}{\sigma^2} \frac{k_0^2 (q-2)^2 \sigma^4}{z^2 \left(1 + \frac{4\sigma^2}{l(z)^2}\right) + k_0^2 (q-2)^2 \sigma^4}\right]. \quad (26)$$

Equation (26) shows the dependence of on-axis average intensity on the combination of various parameters, including input beam waist σ and coherence length $l(z)$. If we omit the factors independent of z , then Eq. (26) can be rewritten as

$$\langle I(0, z) \rangle \approx \frac{z^{q/(2-q)}}{\sqrt{\beta z^2 + \delta}} \exp\left(-\mu \frac{z^{2/(2-q)}}{\beta z^2 + \delta}\right), \quad (27)$$

where $\mu = \left(k_0 \sigma^{2-q} / \alpha q\right)^{2/(q-2)}$, $\beta = 1 + [4\sigma^2 / l(z)^2]$, and $\delta = k_0^2 \sigma^4 (q-2)^2$. From Eq. (27), one can obtain the position of the extremum, which is found from the equation:

$$[(2q-2)\beta z + q\delta z^{-1}](\beta z^2 + \delta) = \mu [(2q-2)\beta z^{(4-q)/(2-q)} + 2\delta z^{[q/(2-q)}]. \quad (28)$$

It should be noted that the expression, Eq. (18), and the more precise expression, Eq. (27), are inapplicable for

From Eq. (23) we can obtain the integral of the form:

$$\iint_{-\infty}^{+\infty} \exp[-(Ax^2 + By^2 + Cxy + Dx + Ey)] dx dy = \frac{\pi}{\sqrt{AB - C^2/4}} \exp\left[\frac{1}{4} \times \frac{AE^2 + BD^2 - CDE}{AB - C^2/4}\right] \quad (24)$$

The expression in Eq. (24) is true if $AB > C^2/4$. In the case under consideration,

$$A = \frac{1}{2\sigma^2} + \frac{1}{l(z)^2} - \frac{i}{2} \frac{\partial^2 \psi(r_0; z)}{\partial r^2},$$

$$B = \frac{1}{2\sigma^2} + \frac{1}{l(z)^2} + \frac{i}{2} \frac{\partial^2 \psi(r_0; z)}{\partial r^2}, \quad C = -\frac{2}{l(z)^2},$$

$$D = ir_0 \frac{\partial^2 \psi(r_0; z)}{\partial r^2}, \quad E = -ir_0 \frac{\partial^2 \psi(r_0; z)}{\partial r^2}. \quad (25)$$

$q = 2$. Therefore, we consider separately the special case for $q = 2$. For $q = 2$, instead of Eq. (8), taking into account the value of the integral over the angle, we obtain

$$\langle I(0, z) \rangle|_{q=2} = \left(\frac{k_0}{z}\right)^2 J_0^2(1) \int_0^\infty \int_0^\infty \exp\left(-\frac{x^2 + y^2}{2\sigma^2}\right) \times \exp\left(-\frac{(x-y)^2}{l(z)^2}\right) \exp\left(\frac{ik_0}{2z}(x^2 - y^2)\right) \times \exp[-i\alpha(x^2 - y^2)] xy dx dy. \quad (29)$$

We simplify Eq. (29) using Eq. (24), choosing the maximum of the modulus of the integrand as the stationary point. After mathematical transformations, we get an explicit form:

$$\langle I(0, z) \rangle|_{q=2} = \left(\frac{k_0}{z}\right)^2 J_0^2(1) \sigma^2 \times \frac{\pi}{\sqrt{(1/4\sigma^4) + [1/l(z)^2 \sigma^2] + [\alpha - (k_0/2z)]^2}}. \quad (30)$$

The maximum will be at $\alpha = k_0/2z$, which corresponds to the lens focus position and coincides with Eq. (2) at $q = 2$. Note that Eq. (30) is obtained by the stationary-phase method, therefore, in principle, it is an approximate solution, for the coherent case $l(z) = \infty$, an exact solution can be obtained.

It is based on the equality

$$\int_0^\infty r \exp(-Ar^2) dr = \frac{1}{2A}. \quad (31)$$

In the coherent case, the integrand in Eq. (29) is separable and we obtain

$$\langle I(0, z) \rangle|_{q=2} = \left(\frac{k_0}{z}\right)^2 J_0^2(1) \frac{1}{4} \frac{1}{(1/4\sigma^4) + [\alpha - (k_0/2z)]^2}. \quad (32)$$

The main difference of Eq. (32) from Eq. (30) is in the absence of the root sign, which is especially pronounced far from the focus. In a partially coherent case, the calculation is more cumbersome, since the function must be made separable. Without giving details, we give the final result, which is similar to both expressions in Eqs. (30) and (32):

$$\langle I(0, z) \rangle|_{q=2} = \left(\frac{k_0}{z}\right)^2 J_0^2(1) \frac{1}{4} \times \frac{1}{(1/4\sigma^4) + [1/l(z)^2\sigma^2] + [\alpha - (k_0/2z)]^2}. \quad (33)$$

Using Eq. (33), it is possible to analytically obtain the autofocusing distance of ALB for fixed values of the coherence length ($l = \text{constant}$):

$$z_{\max} = \frac{k_0\alpha}{2[\alpha^2 + (1/4\sigma^4) + (1/l^2\sigma^2)]}. \quad (34)$$

As can be seen from Eq. (34), if $[(1/4\sigma^4) + (1/l^2\sigma^2)] \ll \alpha^2$, then $z_{\max} = k_0/2\alpha$, which is equal to the lens focus position. This fact allows us to find the approximate position of the maximum for varying coherence length $l(z)$. We calculate first $l_0 = l(z = k_0/2\alpha)$. If $[(1/4\sigma^4) + (1/l_0^2\sigma^2)] \gg \alpha^2$, then the autofocusing distance can be approximately calculated as follows:

$$z_{\max} \approx \frac{k_0}{2\alpha} \left[1 - \frac{1}{\alpha^2} \left(\frac{1}{4\sigma^4} + \frac{1}{l_0^2\sigma^2} \right) \right]. \quad (35)$$

Otherwise, the maximum can be determined from the graph of the function in Eq. (33), as shown in Fig. 1.

Figure 1 shows the behavior of on-axis intensity of ALB as a function of propagation distance in a strong turbulent media. As evident, the plot consists of a peak at $z = 84$ cm, indicating the autofocusing position of ALB. However, in

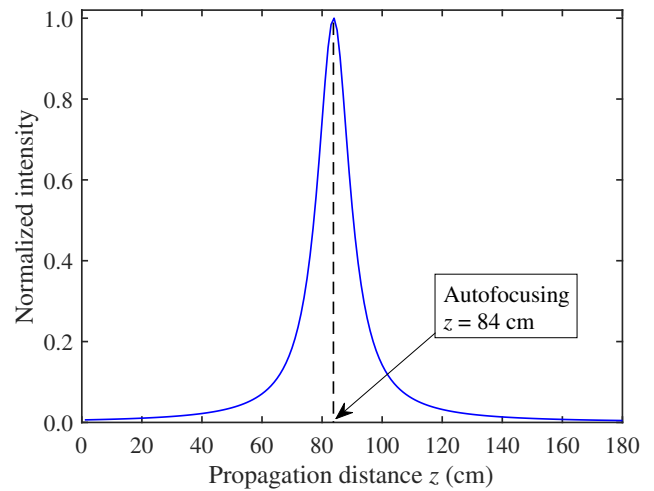


FIG. 1. Variation of on-axis normalized intensity as a function of propagation distance z . The plot is obtained for the following parameters: $\alpha = 3.5 \text{ mm}^{-2}$, $q = 2$, $m = 4$, $\sigma = 1.35 \text{ mm}$, $\lambda = 1064 \text{ nm}$, and $C_n^2 = 10^{-12} \text{ m}^2/3$. The peak value of on-axis intensity indicates the autofocusing position of ALB.

a free space, for the same ALB the autofocusing distance is found to be $z = 84.36$ cm [calculated using Eq. (2)]. It suggests that the autofocusing distance does not show any considerable changes while propagating in a turbulent medium.

III. RESULTS

For a free-space propagation, intensity of an optical field can be calculated (or simulated) by an extended Huygens-Fresnel integral. However, the propagation through an atmosphere needs the involvement of random phase. For ideal considerations, the refractive index of air is taken as nearly unity, but in actual practice random fluctuations of temperature and wind velocity affects the value of refractive index in a random fashion, and induces a considerable effect on the spatial intensity and phase front of an optical field when propagated in the atmosphere. The similar effects also occur when light propagates through any disordered or diffusive media. For the convenience, to examine the effect of atmospheric turbulence on the laser beam, turbulent media is prepared artificially by several methods, such as, aqueous suspension obtained from the mixing of distilled water with insoluble micropowder [38], aerosol optical medium [29], heated aluminum panel with high-power resistors [39], artificial atmospheric and oceanic turbulence, soft biological tissues [36] (and references therein), turbulence chambers consisting of heating elements and fans to create distortions [40], glass plates etched with turbulence phase (turbulent plates), which can be rotated or translated to consider the effect of dynamic turbulence on the laser beam profile [41].

Further, the turbulent medium in the laboratory is also realized by implementing random phase on spatial light modulators (SLMs) and digital micromirror devices (DMDs) [30]. These methods involve more flexibilities, as turbulent strength as well as its phase can be controlled and altered easily. To simulate the random phase screen that can behave like turbulent media of desired strength, various methods are reported, namely, weighted superposition of Zernike polynomials [42], the Monte Carlo method [43], and the subharmonic method [44]. Out of these methods, the Monte Carlo method is considered to be simple and convenient. It generates a random phase screen by using Fourier transform of complex random matrix in spatial frequency domain, whose variance is directly calculated from the von Karman power spectrum and mimics the atmospheric turbulence in the simulations [45,46]. The phase-screen-based approach is further classified into two types: (i) single-phase screen method, and (ii) multiple-phase screen method. The method based on multiple phase screens involves the splitting of desired length (z) of the medium into small intervals Δz , and for each subpart of the medium, a phase screen is prepared and placed at a distance of Δz [33,46]. This method gives good results when the length of the medium is large enough, whereas, for smaller propagation distance in turbulent media, or the case, when thickness of the medium is small as compared to the total propagation length of light beam, a single-phase screen is enough to mimic the turbulent media [30,47]. In our study, the autofocusing distance is in the range of 1 m, so that the single-phase screen approach is used. However, for the propagation of ALB through turbulent media, we perform a comparison between the two approaches, and obtain similar outcomes (see Appendix B).

To analyze the propagation of ALB in a turbulent medium, we simulate a screen consisting of random phase fluctuations that represent a turbulent medium, and impart it on optical field of ALB and propagate further, as shown schematically in Fig. 2. Figure 2 depicts the generation of ALB by illuminating DOE with an input Gaussian beam (laser output), as well as propagation in free space and turbulent media. The turbulence is imparted on the ALB by turbulent phase screen that consists of random fluctuations in the phase distribution.

To simulate the turbulent media, we employ the Monte Carlo method that generates a random phase screen. The variance of random phase function is given by [28,30]

$$\sigma^2(k_x, k_y) = 2\pi k_0^2 z \left(\frac{2\pi}{N\Delta x} \right)^2 \phi_n(k_x, k_y), \quad (36)$$

where Δx denotes grid spacing of $N \times N$ size matrix over which phase screen is generated, and k_x and k_y represent the spatial frequencies over the grid. z denotes distance over which turbulent phase screen is simulated. $\phi_n(k_x, k_y)$ represents a refractive-index power spectrum, which is

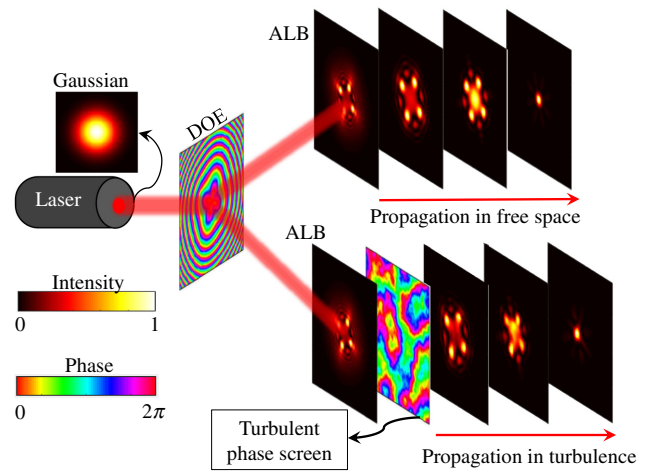


FIG. 2. Schematic illustrating the formation of ALB by illuminating input light from a laser on DOE (phase element), and after that propagated in free space as well as in turbulent media. For the propagation in turbulent media, we impart a random phase distribution on ALB and then propagate.

given as [28,30]

$$\phi_n(k_x, k_y) = 0.33 C_n^2 \frac{\exp(-k^2/k_l^2)}{(k^2 + k_h^2)^{11/6}}, \quad 0 \leq k < \infty, \quad (37)$$

where $k^2 = k_x^2 + k_y^2$ is a radial vector in the spatial frequency domain. $k_l = 5.92/l_0$ and $k_h = 2\pi/L_0$. The l_0 and L_0 denote the size of small- and large-scale eddies. C_n^2 represents the strength of atmospheric turbulence. The values of C_n^2 ranges from $10^{-18} \text{ m}^{2/3}$ for weak turbulence up to $10^{-12} \text{ m}^{2/3}$ for strong turbulence conditions [30]. Now, a $N \times N$ size screen with random phase fluctuations can be generated as

$$\Phi(x, y) = F^{-1}[\text{rand}(k_x, k_y) \times \sigma(k_x, k_y)], \quad (38)$$

where F^{-1} denotes the inverse Fourier transform, and a normal distribution with zero mean and variance one, is used to sample random entries of a complex matrix $\text{rand}(k_x, k_y)$. The simulated phase screens for two different propagation distances are shown in Fig. 3.

Figure 3 clearly shows that although C_n^2 is fixed, but the randomness in the phase distribution can also be varied by changing the propagation distance z . Particularly, a longer propagation in a weak random medium equivalents to a short propagation in a highly random medium.

To analyze the effect of turbulence on ALB, we generate ALB with parameter values $\alpha = 3.5 \text{ mm}^{-2}$, $q = 2$, $m = 4$, $\lambda = 1064 \text{ nm}$, and input beam waist $\sigma = 1.35 \text{ mm}$ (Fig. 2). After that we impose random phase screens with different turbulence strengths on ALB, and then the resulting field is propagated, the results are shown in Fig. 4. Note, the parameter values are chosen for the convenience

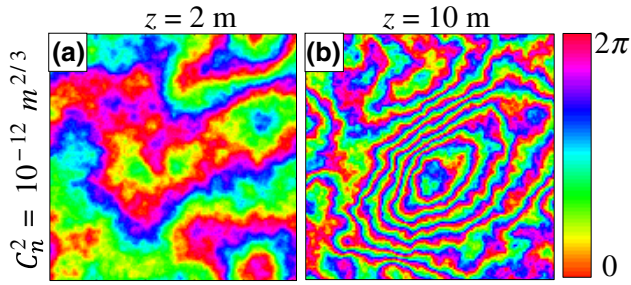


FIG. 3. The random phase screen for (a) $z = 2$ m, and (b) $z = 10$ m, depicting a turbulent medium with different randomness. The results are obtained for a fixed turbulence strength $C_n^2 = 10^{-12} \text{ m}^2/3$, $L_0 = 10$ m, and $l_0 = 0.001$ m.

of analytics and experiment. For example, $\alpha = 3.5 \text{ mm}^{-2}$ provides the autofocusing of ALB in the range of 1 m, suitable for experimental measurements. We also verify numerical results for other values, but obtain similar findings except that the autofocusing distance will change to different values, as well as the lobe structure in ALB will also be different for different m .

Figure 4(a) shows the intensity distribution of a generated ALB at $z = 10$ cm. Figures 4(b)–4(e) present the intensity distribution of ALB at various propagation distances in a free space. As evident the ALB autofocuses at a distance of $z = 85$ cm. Figures 4(f)–4(i) show the

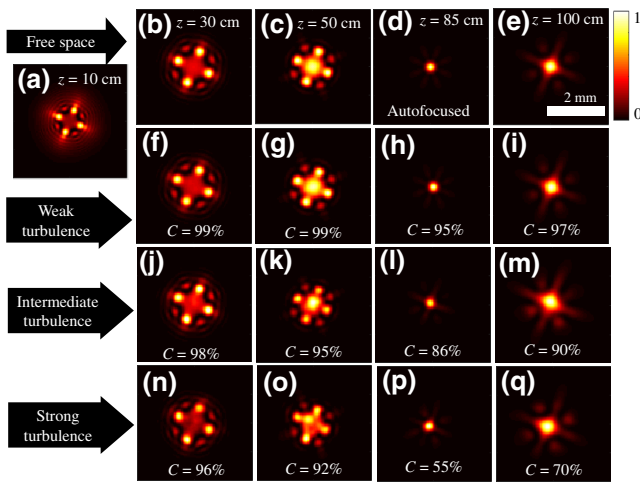


FIG. 4. (a) Intensity distribution of ALB at $z = 10$ cm. The intensity distribution of ALB at various propagation distances in (b)–(e) free space, (f)–(i) weak turbulent medium with $C_n^2 = 10^{-14} \text{ m}^2/3$, (j)–(m) intermediate turbulent medium with $C_n^2 = 10^{-13} \text{ m}^2/3$, and (n)–(q) strong turbulent medium with $C_n^2 = 10^{-12} \text{ m}^2/3$. The results are simulated for the following parameters: $\alpha = 3.5 \text{ mm}^{-2}$, $q = 2$, $m = 4$, $\sigma = 1.35 \text{ mm}$, $\lambda = 1064 \text{ nm}$, $L_0 = 10$ m, and $l_0 = 0.001$ m. For propagation in turbulent media with different strength, the random phase screens are simulated for a propagation length of 2 m.

intensity distribution of ALB at various propagation distances in a weak turbulent medium with $C_n^2 = 10^{-14} \text{ m}^2/3$. The weak turbulence does not affect the ALB significantly, and it again autofocuses at $z = 85$ cm. Figures 4(j)–4(m) show the intensity distribution of ALB at intermediate turbulence strength $C_n^2 = 10^{-13} \text{ m}^2/3$, indicating that the spatial structure is distorted, however, ALB still autofocuses at the same distance $z = 85$ cm. Figures 4(n)–4(q) show the intensity distribution of ALB at various propagation distances in a strong turbulent medium with $C_n^2 = 10^{-12} \text{ m}^2/3$. As evidenced, the spatial structure of ALB is significantly distorted during the propagation. However, the ALB shows autofocusing at the same distance $z = 85$ cm. From these results it is clear that, although the spatial structure of ALB is distorted due to randomness in turbulence, but autofocusing distance remains invariant, indicating the robustness of ALB.

To quantify the effect of turbulence, we calculate an overlap integral, which can be written as [48]

$$C(z) = \frac{\iint I_f(x, y; z) I_t(x, y; z) dx dy}{\sqrt{\iint I_f^2(x, y; z) dx dy \iint I_t^2(x, y; z) dx dy}}, \quad (39)$$

where $I_f(x, y; z)$ and $I_t(x, y; z)$ denote the intensity distributions of ALB in free space and turbulent media, respectively. The calculated values of overlap integral at various propagation distances in turbulent medium are written on the sub figures. As evident, the value of C decreases with increase in randomness of turbulent media (from weak to strong turbulence strength). Further, for a fixed value of C_n^2 (e.g., for strong turbulence) the value of C is approximately 96% at $z = 30$ cm [Fig. 4(n)] and it continues to decrease and becomes minimum ($C = 55\%$) at $z = 85$ cm [Fig. 4(p)], and afterwards it again starts increasing. The decrease in C by increasing turbulence strength can be explained mainly by two reasons: (i) beam wandering and (ii) distortions in the spatial structure of beam. Beam wandering relates to the shifting of beam center and beam trajectory due to insertion of random phase in the path of light, and later is the distortion in the spatial structure of light that happens due to distortion of the actual wave front of ALB, as random phase adds a nonuniform path in various parts of ALB that ends up with overall spatial distortion of the beam.

Figure 5 demonstrates the beam wandering effect as well as the overlap integral as a function of propagation distance z . Figure 5(a) shows the intensity cross section of ALB as a function of z in free space, indicating that ALB autofocuses at $z = 85$ cm. The arrow with the solid blue line marks the central position of unshifted ALB. In Fig. 5(b), the intensity cross section of ALB as a function of z in a strong turbulent medium clearly shows that the ALB still autofocuses at $z = 85$ cm, however, the center of ALB is shifted vertically, as shown by the arrow with

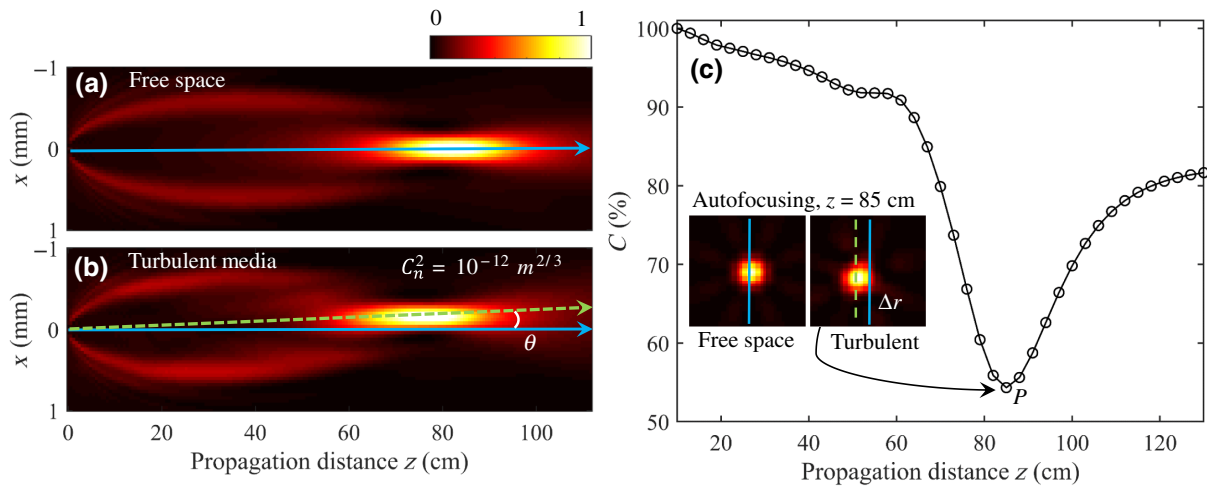


FIG. 5. Intensity cross section of ALB as a function of propagation distance in (a) free space, and (b) turbulent media. (c) The overlap integral as a function of propagation distance. The insets in (c) showing at autofocusing distance, a centred ALB in free space and wandered ALB in turbulent medium. The simulation parameters are kept the same as in Fig. 4. The arrow with the blue solid line marks the central position of unshifted ALB, whereas, the arrow with the green dashed line marks the shifting of central position of ALB due to the wandering effect in turbulence.

the dashed green line. Figure 5(c) shows the overlap C as a function of propagation distance z in a strong turbulent medium. As evident, the overlap decreases with increase in z , and reaches a minimum value at P , and after that it again starts increasing. The point P where C becomes minimum corresponds to an autofocusing position of ALB. The lowest value of C at autofocusing distance can be understood by the fact that most of the energy of ALB is concentrated in a small region, and randomness in the turbulent medium leads to distortion in the spatial structure and beam wandering, which results in a large change in C . The observation of dip with a minimum value of C can also be used to identify the autofocusing distance of ALB. Further, a detailed analysis on dependence of beam wandering on turbulence strength is shown in Appendix A, indicating that the beam wandering becomes more prominent for stronger turbulent medium.

We quantify the findings presented in Fig. 4 for different turbulence strengths, the results are shown in Fig. 6. It is evident from Fig. 6 that for each turbulence strength the minimum of C falls exactly at the same distance, which denotes the same position of autofocusing of ALB. Note, the minimum value of C is found to be different for different turbulence strengths, and can be understood by reasons explained in Fig. 5 and Appendix A.

For the experimental results, ALB is generated by a phase-only spatial light modulator HAMAMATSU-Infrared with a resolution of 800×600 pixels and a pixel size of $20 \mu\text{m}$. An input beam from a laser with wavelength $\lambda = 1064 \text{ nm}$ and diameter approximately 3 mm (see Appendix C) is used to illuminate the DOE phase profile on the SLM, and accordingly after a certain propagation distance ALB is generated. To study the propagation

of ALB in a turbulent medium, we insert an element carrying hot air in the path of ALB [40]. The hot air along the element consists of random fluctuations in temperature and affects the refractive index in a random fashion, which creates an optical turbulence effect. The temperature of the

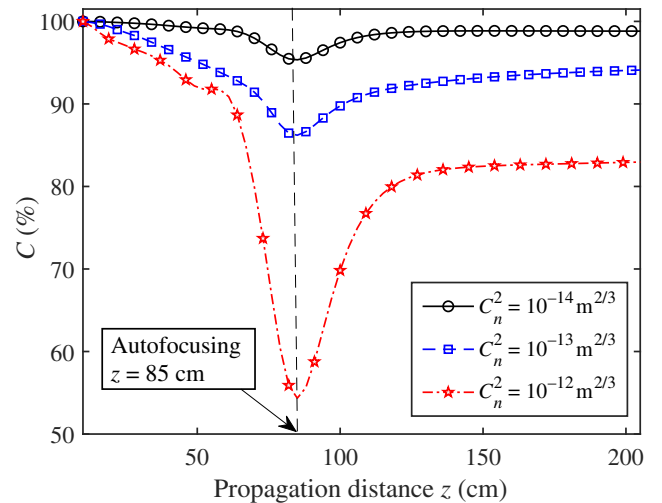


FIG. 6. Overlap integral C as a function of propagation distance z , when ALB is propagated in a turbulent medium with different turbulence strengths. Solid black curve with circles is the weak turbulence with $C_n^2 = 10^{-14} \text{ m}^{2/3}$; dashed blue curve with squares is the intermediate turbulence with $C_n^2 = 10^{-13} \text{ m}^{2/3}$; red dot-dash curve with stars is the strong turbulence with $C_n^2 = 10^{-12} \text{ m}^{2/3}$. Simulation parameters are as follows: $\alpha = 3.5 \text{ mm}^{-2}$, $q = 2$, $m = 4$, $\sigma = 1.35 \text{ mm}$, $\lambda = 1064 \text{ nm}$, $L_0 = 10 \text{ m}$, and $l_0 = 0.001 \text{ m}$. Each phase screen mimics the propagation of ALB in a turbulent medium of length 2 m .

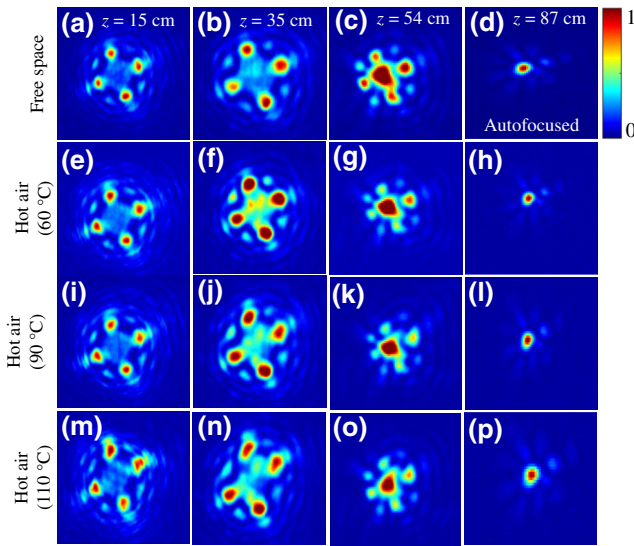


FIG. 7. Experimental results. The intensity distribution of ALB at various propagation distances in (a)–(d) free space, (e)–(h) hot air with temperature 60°C (weak turbulence), (i)–(l) hot air with temperature 90°C (intermediate turbulence), and (m)–(p) hot air with temperature 110°C (strong turbulence). Experimental results are obtained for the following parameters: $\alpha = 3.5 \text{ mm}^{-2}$, $q = 2$, $m = 4$, $\sigma = 1.35 \text{ mm}$, $\lambda = 1064 \text{ nm}$, and input beam diameter = 3 mm .

hot element is stabilized at different values to produce the turbulence of various strengths. The results of propagation of ALB in free space as well as in turbulent medium with different strengths are shown in Fig. 7.

Figures 7(a)–7(d) show the propagation of ALB in a free space, indicating that ALB is autofocused at a distance $z = 87 \text{ cm}$. The results of propagation of ALB through turbulent medium (hot air) with different strengths (different temperatures) are shown in Figs. 7(e)–7(h), 7(i)–7(l), and 7(m)–7(p). As evident, upon increasing the temperature of hot air, the distortion in the spatial intensity distribution of ALB increases. However, at different temperatures, the ALB always autofoci at the same distance $z = 87 \text{ cm}$. This clearly indicates that autofocusing distance of ALB remains invariant, which shows a good agreement with the numerical results. Note that there is a small mismatch between the values of autofocusing distance found in the experiment and simulations, which is anticipated due to the nonideal experimental conditions. Unlike simulations, the input beam in the experiment is not a pure Gaussian (as $M^2 = 1.5$) as well as having different size, see Appendix C.

IV. SPECTRAL DEPENDENCE OF AUTOFOCUSING OF ALB IN A TURBULENT MEDIUM

Spectral properties play a vital role in propagation of optical fields, as spectral variations directly affect the

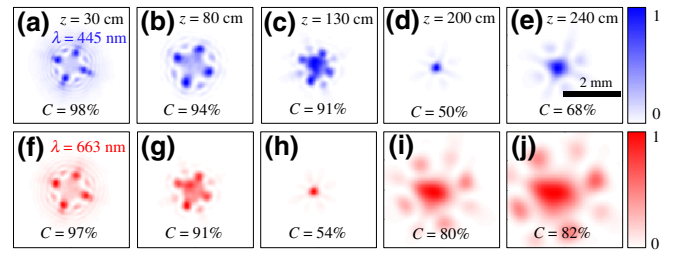


FIG. 8. The intensity distribution of ALB at various propagation distances in a turbulent media for different wavelengths (a)–(e) $\lambda = 445 \text{ nm}$, and (f)–(j) $\lambda = 663 \text{ nm}$. Simulation parameters are as follows: $\alpha = 3.5 \text{ mm}^{-2}$, $q = 2$, $m = 4$, $\sigma = 1.35 \text{ mm}$, $\lambda = 1064 \text{ nm}$, $C_n^2 = 10^{-12} \text{ m}^{-2/3}$, $L_0 = 10 \text{ m}$, and $l_0 = 0.001 \text{ m}$. Phase screen is prepared for propagation of ALB in the turbulent medium of length 2 m .

focusing distance of ALB in free space [18]. It has been shown that the change in the wavelength of ALB has no effect on the spatial intensity distribution, however, it affects the autofocusing distance [Eq. (2)]. Here, we analyze the effect of turbulence on the autofocusing distance when the wavelength of ALB is varied. We impose a turbulent phase screen (as described above) simulated for wavelength $\lambda = 1064 \text{ nm}$ on ALB of different wavelengths, and then analyze its propagation. The results are shown in Fig. 8.

Figures 8(a)–8(e) show the intensity distributions of ALB at various propagation distances in a turbulent media for a wavelength $\lambda = 445 \text{ nm}$. As evident, the spatial intensity distribution of ALB is distorted due to turbulence, however, the ALB autofoci at a distance approximately 200 cm . Figures 8(f)–8(j) show the intensity distribution of ALB in a turbulent media for a wavelength $\lambda = 663 \text{ nm}$. The spatial distortion as well as autofocusing is again observed. However, the autofocusing distance is decreased by approximately 64 cm , and now ALB is focused at $z = 136 \text{ cm}$. The values of C are obtained by calculating the overlap integral [Eq. (39)] between ALBs in turbulent media and their respective ALBs in free space. A detailed plot for C as a function of propagation distance z is shown in Fig. 9. The variation in C can be described with the same reason as given above for Figs. 4 and 5. As evident, for each wavelength a dip with minimum value of C is observed, indicating the value of z corresponding to an autofocusing distance of ALB. For the different wavelengths, the dip occurs at different values of z , indicating the spectral dependence of autofocusing distance. Specifically, the values of autofocusing distances are found to be 85 cm (for $\lambda = 1064 \text{ nm}$), 136 cm (for $\lambda = 663 \text{ nm}$), and 202 cm (for $\lambda = 445 \text{ nm}$). The autofocusing distance decreases with the increase in wavelength. We also calculate the autofocusing distances for propagation of ALBs in a free space using Eq. (2), and find the values of 84.36 cm (for $\lambda = 1064 \text{ nm}$), 135.4 cm (for $\lambda = 663 \text{ nm}$), and 201.7

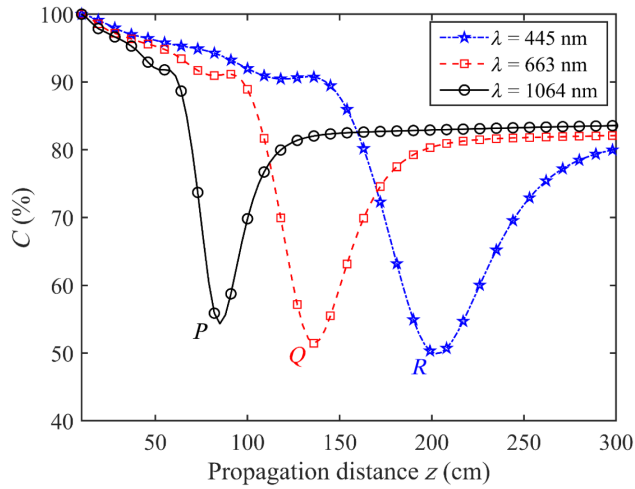


FIG. 9. The overlap integral as a function of propagation distance for different wavelengths $\lambda = 445$ nm (blue dot-dashed curve with stars), $\lambda = 663$ nm (red dashed curve with squares), $\lambda = 1064$ nm (black curve with circles). Points P , Q , and R indicate the autofocusing distances for the respective wavelengths.

cm (for $\lambda = 445$ nm). As evident, the simulated values of autofocusing distances are very close to the theoretical values, which indicates that the spectral dependence of autofocusing distance remains invariant in turbulent media.

V. SELF-HEALING OF ALBS IN FREE SPACE

We investigate the self-healing of ALB in a free space. Specifically, we analyze the effect of various types and amount of truncation of ALBs on their self-healing abilities. For the quantification of self-healing, we calculate the overlap integral [Eq. (39)], which allows identification of the degree of similarity between the original and truncated beam [48]. The ALB is generated by illuminating DOE with an input Gaussian beam at $z = 0$, and then propagated up to a distance $z = 10$ cm, so that ALB is well formed. The ALB is then truncated by an amplitude mask. The original and truncated beams are shown in Figs. 10(a) and 10(f), respectively. The truncation of the main lobes leads to a decrease in the value of the overlap integral to 58% [Fig. 10(f)]. The truncated ALB is then propagated further to analyze the self-healing abilities [Figs. 10(f)–10(j)]. For the comparison and quantification of the overlap integral C , we also propagate nontruncated ALB (ideal case), as shown in Figs. 10(a)–10(e).

As evident, upon propagation of truncated ALB the energy from nearby areas moves into the truncated parts, and thereby it self-heals, as indicated by the complete recovery of the blocked main lobes [Figs. 10(g)–10(j)]. However, as per the conservation of energy, the total energy contained in the beam will be smaller than the nontruncated beam, as a part of the energy is removed by the

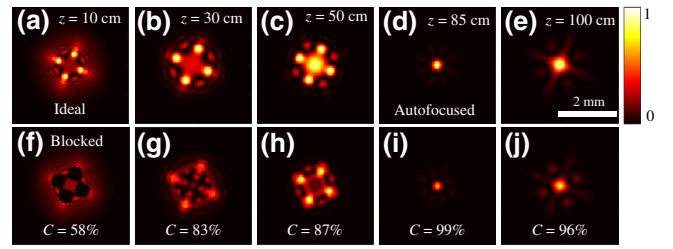


FIG. 10. (a) The intensity distribution of ALB, showing a clear four-lobe structure. (b)–(e) Intensity distribution of ideal ALB (nontruncated) at various propagation distances. (f) Intensity distribution of ALB with truncated lobes. (g)–(j) Intensity distribution of truncated ALB at various propagation distances. C denotes the calculated value of the overlap integral with respect to the ideal case. The parameters for the ALB are $\alpha = 3.5 \text{ mm}^{-2}$, $q = 2$, $m = 4$, $\sigma = 1.35$ mm, and $\lambda = 1064$ nm.

truncation. The energy diffraction efficiency in the truncated beam is reduced to 68% with respect to the ideal ALB. The recovery of truncated lobes is also evidenced by the increased value of the overlap integral. In addition to self-healing, the beam also retains the autofocusing property, as shown in Fig. 10(i). The ALB autofocuses at a distance $z = 85$ cm, and also at this distance the beam completely self-heals, indicated by the maximum value of overlap integral $C = 99.53\%$. The autofocusing distance is found to be the same as in the nontruncated case [Fig. 10(d)], which also agrees with the theoretical value obtained from Eq. (2). Further, we investigate how compound truncation with various percentages affects the self-healing abilities of ALB. The results are shown in Fig. 11. Figures 11(a)–11(e) show the propagation of a truncated beam, in which 20% of the beam area is blocked by an amplitude mask, in free space. As evident, the truncated ALB completely self-heals at the autofocusing

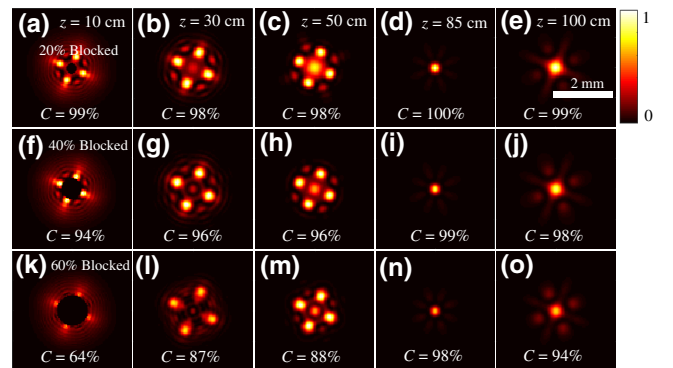


FIG. 11. Self-healing of ALB when various percentages of beam are truncated. Intensity distribution at various propagation distances for the compound truncation of (a)–(e) 20%, (f)–(j) 40%, and (k)–(o) 60%. The corresponding values of the overlap integral are written on them. The parameters for the ALB are $\alpha = 3.5 \text{ mm}^{-2}$, $q = 2$, $m = 4$, $\sigma = 1.35$ mm, and $\lambda = 1064$ nm.

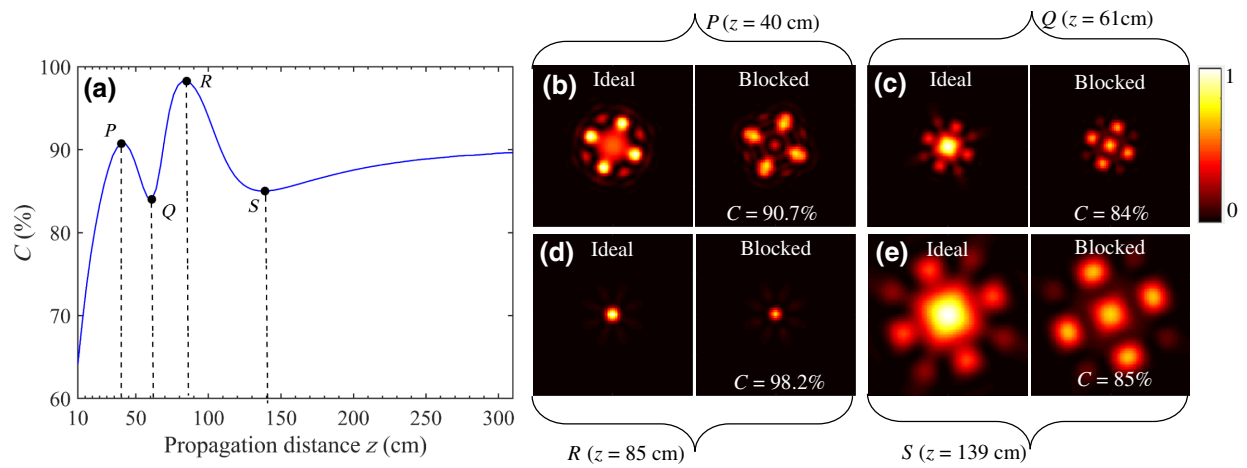


FIG. 12. (a) The overlap integral as a function of propagation distance for 60% of compound truncation. (b)–(e) The intensity distributions of truncated ALB together with the ideal nontruncated ALB, corresponding to points P , Q , R , and S . The parameters for the ALB are $\alpha = 3.5 \text{ mm}^{-2}$, $q = 2$, $m = 4$, $\sigma = 1.35 \text{ mm}$, and $\lambda = 1064 \text{ nm}$.

distance $z = 85 \text{ cm}$ [Figs. 11(a)–11(e)], indicated by the maximum value of overlap C . The propagation of ALBs with 40% and 60% of truncations also shows that the maximum self-healing occurs at autofocusing distance $z = 85 \text{ cm}$, which is evident from the maximum values of overlap C [Figs. 11(f)–11(j) and Figs. 11(k)–11(o)]. From these results it is clear that truncation of ALB does not affect the autofocusing distance as well as the self-healing distance. The self-healing can be understood by the fact that during the propagation of truncated beam, the energy self-redistributes and flows towards the truncated parts, and slowly attains its original shape.

We also calculate the overlap C as a function of propagation distance for various percentages of compound truncation, as shown in Fig. 12. It is found that the value of C increases with distance z , and reaches a maximum value, and after that it again starts decreasing. The peak with highest C [marked by R in Fig. 12(a)] indicates a position at which truncated ALB recovers well, and shows maximum similarity with the ideal (original) beam at that propagation distance. Note that for the higher percentages of truncation, the value of C also becomes relatively smaller. The observation of another lower peak at P and minima at Q and S can be explained as follows. In free space, when a partially blocked ALB propagates, the self-healing occurs due to the fact that different parts of the ALB interfere upon propagation and redistribution of intensity takes place. Because of this, the spatial intensity distribution of ALB changes, which results in a change in the values of overlap integral [marked by P , Q , and S in Fig. 12(a)]. However, at the autofocusing distance, the ALB recovers maximally and a significant portion of intensity is tightly focused at the center, and thus shows a high degree of similarity (high overlap integral value,

marked by R) with an ideal ALB (unblocked ALB). After the autofocusing, upon further propagation the ALB defocuses and redistribution of intensity further takes place that results in the change of spatial intensity distribution of ALB, and thus the value of the overlap integral again changes. Finally, when the spatial intensity distribution becomes stable, the overlap integral attains a constant value.

As evident, corresponding to points P , Q , R , and S [in Fig. 12(a)], Figs. 12(b)–12(e) show that the ideal and blocked beams have different spatial intensity distributions and therefore the value of C is different. After point S , the spatial intensity distribution of ALB changes slowly and tends to stabilize, and thus the value of C varies slowly and tends to approach a fixed value.

Furthermore, these beams (ALBs) show some other advantages, such as, the self-healing distance is independent of the amount of truncation of ALB (as the self-healing reaches its maximum value for the same value of the propagation distance, i.e., autofocusing distance), which makes them different from the other beams exhibiting self-healing property.

Further, we verify the autofocusing distance by analyzing the intensity of ALB at the center (on axis), as it should increase to a maximum value at the autofocusing distance. Figure 13 shows the cross section of on-axis intensity of ALB as a function of propagation distance for various percentage of compound truncation. For the comparison, we also include results for a nontruncated ALB. The on-axis intensities of truncated beams are normalized with respect to the nontruncated beam (solid black curve). As evidenced, for all the cases of truncation the on-axis intensity becomes maximum (peak value) at $z = 85 \text{ cm}$ [which is the autofocusing distance of a

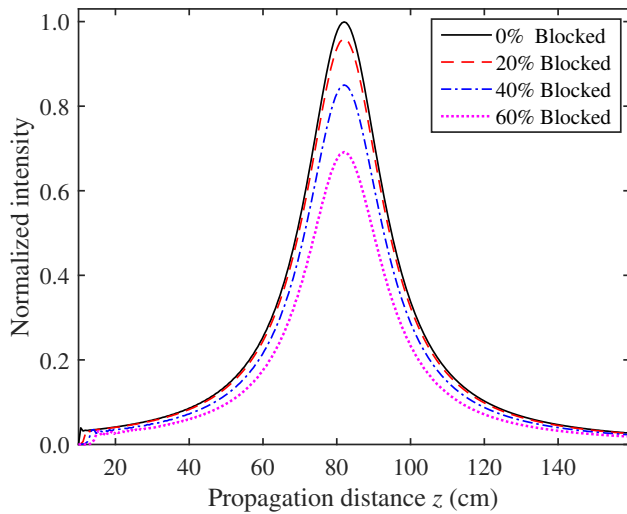


FIG. 13. Cross section of on-axis intensity of ALB as a function of propagation distance, for the various percentages of compound truncation.

nontruncated ALB, Fig. 10(d)], indicating that the truncation of ALB does not affect the autofocusing distance. The on-axis intensity at the autofocusing distance decreases with the increase of truncation, but the autofocusing properties remains invariant even after a large truncation of ALB (60%). These results clearly indicate that even if a major part of the beam is truncated, the ALBs do possess a self-healing property. Also the truncation has no effect on the autofocusing distance of ALBs, indicating good robustness of ALBs.

To verify the simulation results of self-healing of ALB in free space, we perform an experiment with the same parameter values. In the experiment, we use a binary mask to truncate the approximately 25% area of ALB (compound truncation) around the center, which is kept at a distance of approximately 10 cm from the SLM. The truncated ALB is propagated further and intensity distribution is recorded at various propagation distances. The results are shown in Fig. 14. For the comparison, we also

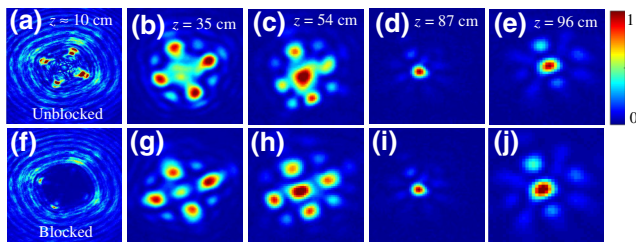


FIG. 14. Experimental results of self-healing of ALB in free space, when the approximately 25% area of ALB is truncated around the center. The parameters for the ALB are $\alpha = 3.5 \text{ mm}^{-2}$, $q = 2$, $m = 4$, $\sigma = 1.35 \text{ mm}$, and $\lambda = 1064 \text{ nm}$.

record intensity distribution of an ideal ALB (nontruncated) at various propagation distances [Figs. 14(a)–14(e)]. Figures 14(f)–14(j) show the intensity distribution of a truncated ALB at various propagation distances, which indicates that truncated ALB self-heals as well as autofocuses. In both cases autofocusing is observed at the same distance $z = 87 \text{ cm}$. The experimental results show good agreement with the simulations, which further confirms the self-healing abilities of ALB.

VI. SELF-HEALING IN A TURBULENT MEDIA

We also investigate the self-healing abilities of ALBs in a turbulent medium, the results are shown in Fig. 15. The ALB is considered with the same parameters as in Fig. 10, and then truncated differently by amplitude masks [Figs. 15(a) and 15(f)]. Figures 15(b)–15(e) show the propagation in a strong turbulent medium with $C_n^2 = 10^{-12} \text{ m}^2/3$, when the main lobes of the ALB are truncated. In contrast, Figs. 15(g)–15(j) show the propagation of a compound-truncated ALB in the same turbulent media. The C values in Figs. 15(a) and 15(f) show that the percentage of truncation is not the same in both cases. As evident, in both cases the truncated parts of the ALBs recover upon propagation. However, as compared to Figs. 10 and 11, the spatial structure of ALB is distorted due to turbulent medium. The truncated ALBs show the autofocusing at a distance approximately 85 cm. As explained for the free-space propagation in Figs. 10 and 11, the self-healing becomes maximum at autofocusing distance. In a turbulent medium, the maximum self-healing also occurs at the autofocusing distance. However, unlike the case in free space, a minimum value of the overlap integral is observed at the autofocusing distance due to beam wandering effect, where tightly focused energy beam is shifted from its original position, and distortion occurs in the spatial structure of ALB due to the presence of randomness in the phase

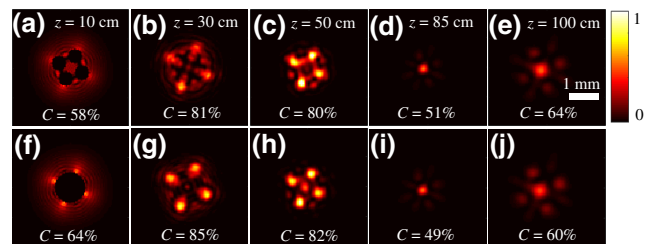


FIG. 15. The self-healing of ALBs in a turbulent media. (a)–(e) Intensity distribution at various distances, when a lobe-truncated ALB is propagated in turbulent media of strong turbulence strength. (f)–(j) Intensity distribution at various distances, when compound-truncated ALB is propagated in turbulent media of the same strength. Simulation parameters are as follows: $\alpha = 3.5 \text{ mm}^{-2}$, $q = 2$, $m = 4$, $\sigma = 1.35 \text{ mm}$, $\lambda = 1064 \text{ nm}$, $C_n^2 = 10^{-12} \text{ m}^2/3$, $L_0 = 10 \text{ m}$, and $l_0 = 0.001 \text{ m}$.

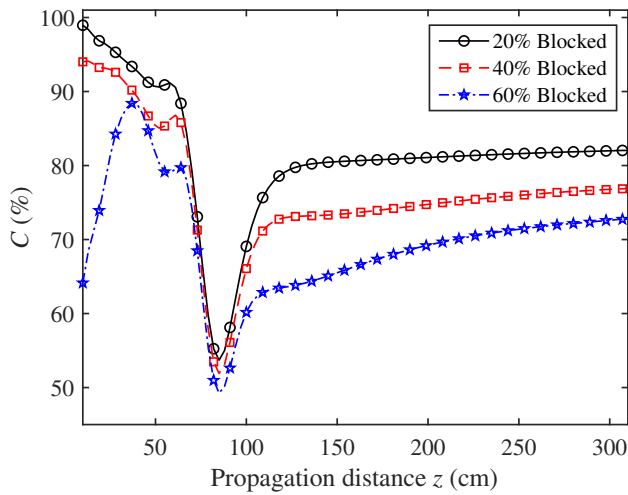


FIG. 16. The variation of overlap C as a function of propagation distance for the various percentages of compound truncation.

(Appendix A). Further propagation after the autofocusing distance again leads to the defocusing of beam, and due to its large size, the beam exhibits more overlap with the non-truncated beam (at $z = 100$ cm), and hence an increased value of C is observed.

In a strong turbulent medium with $C_n^2 = 10^{-12} \text{ m}^2/3$, we also analyze the self-healing of ALB with different percentages of compound truncation. The results are shown in Fig. 16. It is evidenced that ALB self-heals reasonably well for a compound truncation up to 60%. We also check for the increased compound truncation up to 80% (not shown here), it is observed that ALB still can self-heal quite well.

Figure 16 shows the overlap C as a function of z for the various percentages of compound truncation of ALB. Again, a dip with a minimum value of C is observed at the same distance, corresponding to an autofocusing

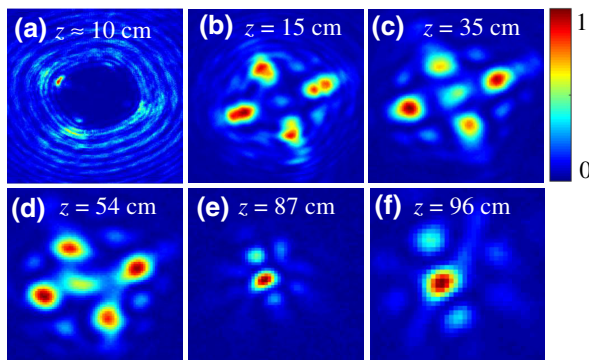


FIG. 17. Experimental results. (a) Intensity distribution of truncated ALB. (b)–(f) Intensity distribution of truncated ALB at various propagation distances in a turbulent media (hot air at 110°C).

distance of nontruncated ALB [Fig. 10(d)]. At this distance the compound-truncated ALB exhibits a maximum self-healing.

We also record experimental results of self-healing of ALB in a turbulent medium. To do that we truncate the approximately 25% area of ALB from the center [Fig. 17(a)], and then propagate through hot air at temperature 110°C [Figs. 17(b)–17(f)]. As evident, truncated ALB self-heals upon propagation as well as autofocuses at a distance of $z = 87$ cm, which shows a good qualitative agreement with numerical results (Fig. 15). We again observe the distortions in the spatial structure of ALB upon propagation, which is caused by the randomness in the turbulence.

VII. CONCLUSIONS

We present the effect of turbulence on propagation (autofocusing) and self-healing properties of ALBs. We find that the autofocusing properties of ALBs do not depend on the turbulent medium, however, turbulence causes the distortions in the spatial intensity distribution of ALBs. The spectral dependence of autofocusing distance also remains invariant in the turbulent media. The results show that the self-healing of ALBs occurs in both free space as well as in turbulent media. In particular, self-healing distance is found to be the same as autofocusing distance. It is also found that when a large portion of ALB (around 60%) is truncated, the beam is still able to self-heal reasonably well. Further, for different percentages of truncation the self-healing distance remains the same. The ALBs are found to exhibit great robustness against truncation, which can be applicable in various fields.

Unlike autofocused beams reported earlier, such as pin-like optical beams [2,3], and abruptly autofocused beams [1,5,35], our work presents several advances: (i) easy control on lobe structure of ALB and autofocusing distance (from small to large values), (ii) self-healing in free space as well as in turbulent media, (iii) invariance of self-healing distance against truncation in both free space as well as in turbulent media, (iv) invariance of autofocusing distance under turbulence, and (v) turbulence does not affect the spectral dependence of autofocusing distance.

With these unique characteristics, we believe that our findings can be potentially exploited for a wide range of applications. For example, robustness against turbulence and obstructions makes them useful for optical communications in free space and turbulent atmosphere [2–4]. As the autofocusing forms a tightly focused spot with maximum power, and with the ability to control the autofocusing distance from small to large values, these beams are potentially useful for surgery and ablation applications [1]. These beams with good self-healing abilities in free space and turbulent media, may widely be used in imaging and investigation of the biomedical materials

and to examine small complex biological samples or tissues, trapping and guiding microparticles, and material processing [1,3,5].

ACKNOWLEDGMENTS

An ISIRD Grant from the Indian Institute of Technology (IIT) Ropar (Grant No. 9-230/2018/IITRPR/3255) is acknowledged. Vasu Dev acknowledges the fellowship support by IIT Ropar. Andra Naresh Kumar Reddy gratefully acknowledges the Feinberg Graduate School post-doctoral fellowship, Weizmann Institute of Science, Israel, that has supported the research. This work is also partly funded by the Russian Foundation for Basic Research under Grant No. 20-07-00505 and the Ministry of Science and Higher Education within the government project of FSRC “Crystallography and Photonics” RAS under Agreement No. 007-GZ/Ch3363/26 (theoretical part).

APPENDIX A: BEAM WANDERING

Here, we show beam wandering effects on propagation of ALB in the turbulent media of different strengths (Fig. 18). Beam wandering of ALB in turbulent media is analyzed by considering 40 realizations of random phase screens (for each turbulent strength) to obtain more reliable results. It is evident that for a fixed turbulence strength, beam wander increases as beam propagates through the turbulent medium. Further, beam wander becomes more prominent for stronger turbulence strength.

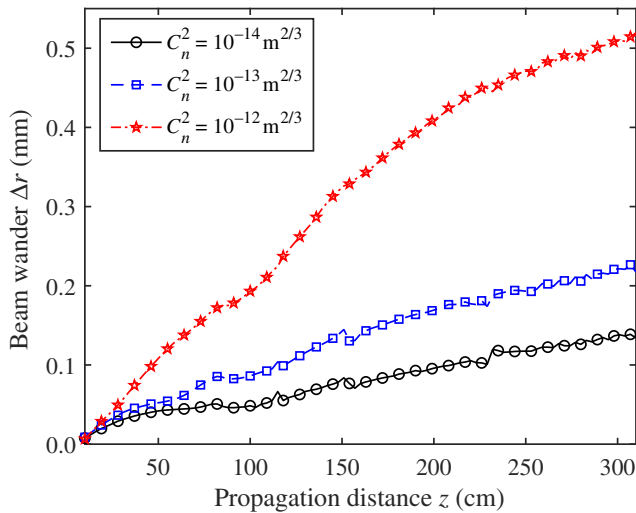


FIG. 18. Beam wandering as a function of propagation distance z , when ALB is propagated in a turbulent medium with various turbulence strengths. Simulation parameters are $\alpha = 3.5 \text{ mm}^{-2}$, $q = 2$, $m = 4$, $\sigma = 1.35 \text{ mm}$, $\lambda = 1064 \text{ nm}$, $L_0 = 10 \text{ m}$, and $l_0 = 0.001 \text{ m}$. For propagation in turbulent media with different strength, the random phase screens are simulated for a propagation length of 2 m.

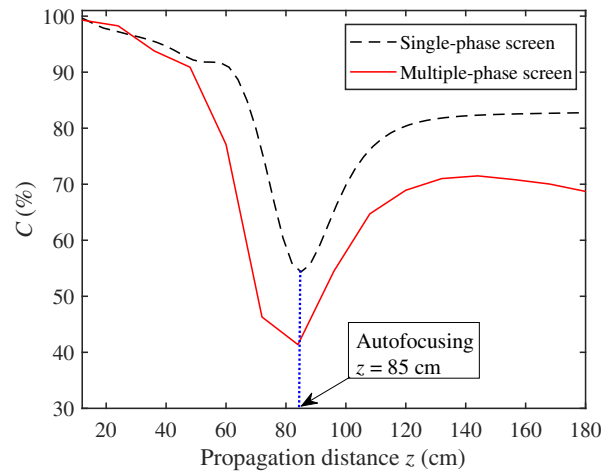


FIG. 19. Comparison of results obtained from the single-phase screen method (black dashed curve) and multiple-phase screen method (solid red curve). Simulation parameters are as follows: $\alpha = 3.5$, $q = 2$, and $C_n^2 = 10^{-12} \text{ m}^{-2/3}$.

APPENDIX B: COMPARISON BETWEEN SINGLE-PHASE AND MULTIPLE-PHASE SCREEN METHOD

Here, we compare the results obtained on the propagation of the ALB in turbulent media based on single-phase screen and multiple-phase screen methods. For the single-phase screen method, a turbulent phase screen is created for a propagation length of 1.8 m, representing a turbulent medium of length 1.8 m. The ALB is propagated through this turbulent medium, and the overlap integral is calculated with respect to the free-space propagation, the results are shown in Fig. 19. For the single-phase screen method (black dashed curve), a dip is observed at a distance $z = 85 \text{ cm}$, which confirms the autofocusing of ALB (also see Fig. 6). In the second method of multiple-phase screen, several phase screens are prepared corresponding to $\Delta z = 12 \text{ cm}$, and placed in the path of ALB at equal intervals. The obtained results are shown by the solid red curve in Fig. 19. Again, a dip is observed at the same autofocusing distance ($z = 85 \text{ cm}$), and provides similar information as obtained from the single-phase screen method.

APPENDIX C: QUALITY OF INPUT LASER BEAM

For the experimental study, we use a cw laser at wavelength $\lambda = 1064 \text{ nm}$. The laser output consists of an intensity distribution whose beam quality factor is $M^2 = 1.5$, indicating a deviation from a pure Gaussian beam (Fig. 20). This input beam is used to illuminate the DOE (size = 3.5 mm) imposed on the SLM for the generation of ALB.

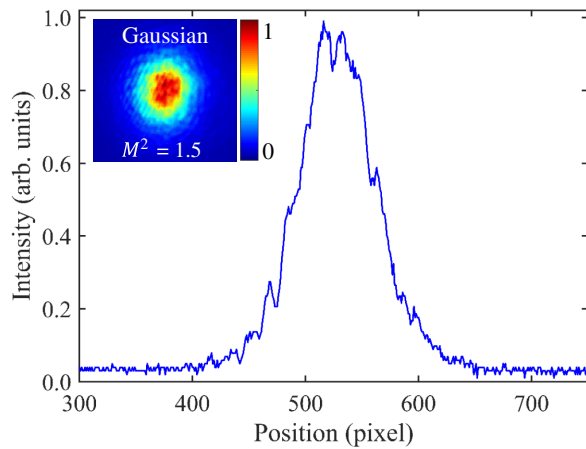


FIG. 20. Intensity cross section of the laser output (input beam). Inset shows the two-dimensional intensity distribution of the laser output with a calculated value of $M^2 = 1.5$.

- [1] D. G. Papazoglou, N. K. Efremidis, D. N. Christodoulides, and S. Tzortzakakis, Observation of abruptly autofocusing waves, *Opt. Lett.* **36**, 1842 (2011).
- [2] Z. Zhang, X. Liang, M. Goutsoulas, D. Li, X. Yang, S. Yin, J. Xu, D. N. Christodoulides, N. K. Efremidis, and Z. Chen, Robust propagation of pin-like optical beam through atmospheric turbulence, *APL Photonics* **4**, 076103 (2019).
- [3] D. Li, D. Bongiovanni, M. Goutsoulas, S. Xia, Z. Zhang, Y. Hu, D. Song, R. Morandotti, N. K. Efremidis, and Z. Chen, Direct comparison of anti-diffracting optical pin beams and abruptly autofocusing beams, *OSA Continuum* **3**, 1525 (2020).
- [4] X. Yan, L. Guo, M. Cheng, and J. Li, Controlling abruptly autofocusing vortex beams to mitigate crosstalk and vortex splitting in free-space optical communication, *Opt. Express* **26**, 12605 (2018).
- [5] P. Zhang, J. Prakash, Z. Zhang, M. S. Mills, N. K. Efremidis, D. N. Christodoulides, and Z. Chen, Trapping and guiding microparticles with morphing autofocusing airy beams, *Opt. Lett.* **36**, 2883 (2011).
- [6] M. Born, E. Wolf, A. B. Bhatia, P. C. Clemmow, D. Gabor, A. R. Stokes, A. M. Taylor, P. A. Wayman, and W. L. Wilcock, *Principles of Optics: Electromagnetic Theory of Propagation, Interference and Diffraction of Light* (Cambridge University Press, Cambridge, United Kingdom, 1999), 7th ed.
- [7] M. J. Booth, Adaptive optical microscopy: The ongoing quest for a perfect image, *Light Sci. Appl.* **3**, e165 (2014).
- [8] A. N. K. Reddy, D. K. Sagar, and S. N. Khonina, Asymmetric apodization for the comma aberrated point spread function, *Comput. Opt.* **41**, 484 (2017).
- [9] A. N. K. Reddy, M. Hashemi, and S. N. Khonina, Apodization of two-dimensional pupils with aberrations, *Pramana* **90**, 77 (2018).
- [10] S. Khonina, A. Ustinov, and E. Pelevina, Analysis of wave aberration influence on reducing focal spot size in a high-aperture focusing system, *J. Opt.* **13**, 095702 (2011).
- [11] R. Kant, Superresolution and increased depth of focus: An inverse problem of vector diffraction, *J. Mod. Opt.* **47**, 905 (2000).
- [12] S. N. Khonina, A. V. Ustinov, and S. Chavez-Cerda, Generalized parabolic nondiffracting beams of two orders, *J. Opt. Soc. Am. A* **35**, 1511 (2018).
- [13] J. Serna, F. Encinas-Sanz, and G. Nemes, Complete spatial characterization of a pulsed doughnut-type beam by use of spherical optics and a cylindrical lens, *J. Opt. Soc. Am. A* **18**, 1726 (2001).
- [14] S. Khonina, V. Kotlyar, V. Soifer, K. Jefimovs, P. Pääkkönen, and J. Turunen, Astigmatic Bessel laser beams, *J. Mod. Opt.* **51**, 677 (2004).
- [15] A. Dixit, S. K. Mishra, and A. K. Gupta, Sensitivity of singular beams in the presence of Zernike aberrations, *Opt. Lasers Eng.* **71**, 74 (2015).
- [16] S. Topuzoski and L. Janicijevic, Diffraction characteristics of optical elements designed as phase layers with cosine-profiled periodicity in the azimuthal direction, *J. Opt. Soc. Am. A* **28**, 2465 (2011).
- [17] S. N. Khonina, A. V. Ustinov, and A. P. Porfirev, Aberration laser beams with autofocusing properties, *Appl. Opt.* **57**, 1410 (2018).
- [18] A. N. K. Reddy, S. N. Khonina, and V. Pal, Generating autofocused aberration laser beams with different spectral performance, *J. Opt.* **22**, 045606 (2020).
- [19] A. Kovalev, V. Kotlyar, and A. Porfirev, Auto-focusing accelerating hyper-geometric laser beams, *J. Opt.* **18**, 025610 (2016).
- [20] I. Chremmos, N. K. Efremidis, and D. N. Christodoulides, Pre-engineered abruptly autofocusing beams, *Opt. Lett.* **36**, 1890 (2011).
- [21] J. D. Ring, J. Lindberg, A. Mourka, M. Mazilu, K. Dhollakia, and M. R. Dennis, Auto-focusing and self-healing of Pearcey beams, *Opt. Express* **20**, 18955 (2012).
- [22] N. K. Efremidis and D. N. Christodoulides, Abruptly autofocusing waves, *Opt. Lett.* **35**, 4045 (2010).
- [23] J. A. Davis, D. M. Cottrell, and D. Sand, Abruptly autofocusing vortex beams, *Opt. Express* **20**, 13302 (2012).
- [24] A. Lagendijk and B. A. Van Tiggelen, Resonant multiple scattering of light, *Phys. Rep.* **270**, 143 (1996).
- [25] P. Sebbah, *Waves and Imaging through Complex Media* (Springer Science & Business Media, Cargese, France, 2001).
- [26] T. Schwartz, S. Fishman, and M. Segev, Localisation of light in disordered lattices, *Electron. Lett.* **44**, 165 (2008).
- [27] K. G. Makris, A. Brandstötter, P. Ambichl, Z. H. Muslimani, and S. Rotter, Wave propagation through disordered media without backscattering and intensity variations, *Light Sci. Appl.* **6**, e17035 (2017).
- [28] L. C. Andrews and R. L. Phillips, *Laser Beam Propagation through Random Media* (SPIE, Bellingham, Washington, USA, 2005).
- [29] A. P. Porfirev, M. S. Kirilenko, S. N. Khonina, R. V. Skidanov, and V. A. Soifer, Study of propagation of vortex beams in aerosol optical medium, *Appl. Opt.* **56**, E8 (2017).
- [30] M. A. Cox, N. Mphuthi, I. Nape, N. Mashaba, L. Cheng, and A. Forbes, Structured light in turbulence, *IEEE J. Sel. Top. Quantum Electron.* **27**, 7500521 (2021).

- [31] V. P. Lukin, P. A. Konyaev, and V. A. Sennikov, Beam spreading of vortex beams propagating in turbulent atmosphere, *Appl. Opt.* **51**, C84 (2012).
- [32] I. P. Lukin, Mean intensity of vortex Bessel beams propagating in turbulent atmosphere, *Appl. Opt.* **53**, 3287 (2014).
- [33] G. Gbur and R. K. Tyson, Vortex beam propagation through atmospheric turbulence and topological charge conservation, *J. Opt. Soc. Am. A* **25**, 225 (2008).
- [34] X. Chu, Evolution of an airy beam in turbulence, *Opt. Lett.* **36**, 2701 (2011).
- [35] W. Lu, X. Sun, H. Chen, S. Liu, and Z. Lin, Abruptly autofocusing property and optical manipulation of circular airy beams, *Phys. Rev. A* **99**, 013817 (2019).
- [36] V. A. Soifer, O. Korotkova, S. N. Khonina, and E. A. Shchepakina, Vortex beams in turbulent media, *Comput. Opt.* **40**, 605 (2016).
- [37] M. Alavinejad, B. Ghafary, and F. Kashani, Analysis of the propagation of flat-topped beam with various beam orders through turbulent atmosphere, *Opt. Lasers Eng.* **46**, 1 (2008).
- [38] S. Khonina, S. Karpeev, and V. Parani, A technique for simultaneous detection of individual vortex states of Laguerre–Gaussian beams transmitted through an aqueous suspension of microparticles, *Opt. Lasers Eng.* **105**, 68 (2018).
- [39] S. M. Augustine and N. Chetty, Experimental verification of the turbulent effects on laser beam propagation in space, *Atmosfera* **27**, 385 (2014).
- [40] H. Gamo and A. K. Majumdar, Atmospheric turbulence chamber for optical transmission experiment: Characterization by thermal method, *Appl. Opt.* **17**, 3755 (1978).
- [41] T. A. Rhoadarmer and J. R. P. Angel, Low-cost, broadband static phase plate for generating atmospheric-like turbulence, *Appl. Opt.* **40**, 2946 (2001).
- [42] R. J. Noll, Zernike polynomials and atmospheric turbulence, *J. Opt. Soc. Am. A* **66**, 207 (1976).
- [43] B. L. McGlamery, Restoration of turbulence-degraded images, *J. Opt. Soc. Am. A* **57**, 293 (1967).
- [44] R. Lane, A. Glindemann, and J. Dainty, Simulation of a Kolmogorov phase screen, *Waves Random Media* **2**, 209 (1992).
- [45] J. Schmidt, *Numerical Simulation of Optical Wave Propagation with Examples in MATLAB* (SPIE, Bellingham, Washington, USA, 2010).
- [46] Y. Zhang, D. Ma, Z. Zhou, and X. Yuan, Research on partially coherent flat-topped vortex hollow beam propagation in turbulent atmosphere, *Appl. Opt.* **56**, 2922 (2017).
- [47] L. Burger, I. A. Litvin, and A. Forbes, Simulating atmospheric turbulence using a phase-only spatial light modulator, *S. Afr. J. Sci.* **104**, 129 (2008).
- [48] R. Chriki, G. Barach, C. Tradosny, S. Smartsev, V. Pal, A. A. Friesem, and N. Davidson, Rapid and efficient formation of propagation invariant shaped laser beams, *Opt. Express* **26**, 4431 (2018).